



CHORUS

This is the accepted manuscript made available via CHORUS. The article has been published as:

Chemomechanics control of tearing paths in graphene

Xu Huang, Hui Yang, Adri C. T. van Duin, K. Jimmy Hsia, and Sulim Zhang

Phys. Rev. B **85**, 195453 — Published 25 May 2012

DOI: [10.1103/PhysRevB.85.195453](https://doi.org/10.1103/PhysRevB.85.195453)

Chemo-mechanical Control of Tearing Paths in Graphene

Xu Huang¹, Hui Yang¹, Adri van Duin², K. Jimmy Hsia³, Sulin Zhang^{1,*}

¹*Department of Engineering Science and Mechanics,
Pennsylvania State University, University Park, PA 16802, USA*

²*Department of Mechanical and Nuclear Engineering,
Pennsylvania State University, University Park, PA 16802, USA and*

³*Department of Mechanical Science and Engineering, University of Illinois, Urbana, IL 61801, USA*

(Dated: May 8, 2012)

Owing to its molecular membrane structure, tearing is the predominant fracture mode for a monolayer graphene. Yet the tearing mechanics of monolayer graphene as a two-dimensional (2D) crystal remains poorly understood. Here, we performed molecular dynamics (MD) simulations with reactive force field (ReaxFF) to determine the fracture path of monolayer graphene under tearing. Our simulations revealed that the tearing chemo-mechanical conditions play a regulatory role on the edge structures of graphene nanoribbons (GNRs) produced by tearing. In vacuum, the resulting GNR features the armchair edge, whereas in the presence of chemical additives (such as oxygens) to the fracture surface the resulting GNR edge changes from armchair to zigzag. In addition, due to the large in-plane stretching to out-of-plane bending stiffness ratio of monolayer graphene, tearing causes local bending at the crack tip, giving rise to a fracture mode mixity that also modulates the fracture path. In addition to provide an atomistic understanding of tearing mechanics of 2D crystal membranes, our findings shed light on chemo-mechanical engineering of GNRs with controlled edge structures.

PACS numbers: 61.72.-y, 61.50.Ah, 62.20.-x, 68.65.-k

I. I. INTRODUCTION

Graphene, an atomic layer of carbon atoms arranged in a honeycomb lattice, has attracted much attention because of its unusual fundamental physical phenomena such as unconventional quantum Hall effects and surprisingly high room-temperature electron mobility¹⁻³. The discovery of these novel physical properties has inspired an endeavor that may lead to the establishment of next-generation graphene-based electronics in replacing current silicon technologies. In order for graphene to present a sizable energy gap for electronic applications, a key requirement in graphene fabrication is that the width of graphene should be as small as $\sim 10\text{nm}$ ⁴. For such graphene nano-ribbons (GNRs), the edge orientation strongly influences their electronic properties⁵⁻⁷. Atomic edge engineering⁸⁻¹⁰ has therefore emerged as an effective means to control the electronic performance of GNR-based devices.

Given the current unique capabilities in nanoscale manipulation of graphene by experimentalists^{11,12}, GNRs could be prepared by simply tearing from a large pristine graphene sheet. Yet the tearing response of monolayer graphene as a two-dimensional (2D) crystal and the edge structures of the produced GNRs are poorly understood from a fundamental mechanics perspective. Here we demonstrate from faithful molecular dynamics (MD) simulations that the edge orientation of GNRs torn off from a pristine monolayer graphene can be modulated by the chemo-mechanical tearing conditions. In particular, our atomistic simulations showed that chemical additives to the fracture surface modify the fracture resistance to an extent depending on the crystallographic orientations. Our analysis further evidenced that owing to the unique molecular membrane structure of monolayer graphene, tearing inevitably induces out-of-plane bending at the crack tip, introducing fracture mode mixity that may cause crack kinking. Together, these two factors set the energetically and kinetically preferred fracture path. We expect that the regulatory mechanism provides valuable guidance to the production of GNRs with precisely controlled edge orientation. Besides providing a general atomistic framework for predicting fracture path in crystals, our studies offer atomistic understanding of fracture behavior of 2D crystal membranes. Given the intimate relationship between GNR edge orientation and its electronic structures, our findings also have important implications for the next-generation graphene-based electronic devices.

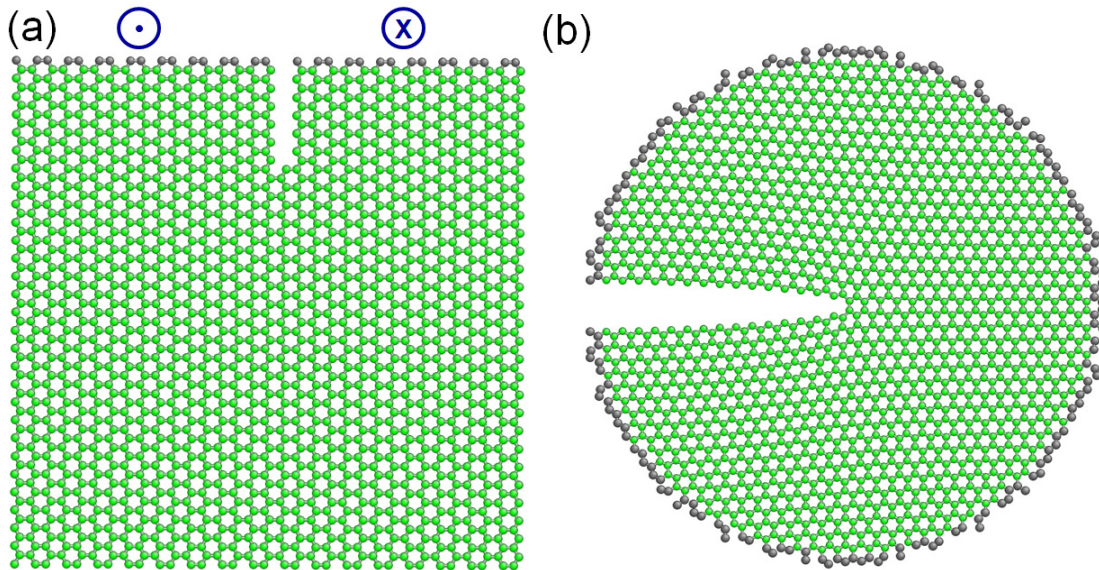


FIG. 1: The simulation models. (a) The finite-sized crack model. Edge atoms in grey are fixed and subjected to out-of-plane pulling with directions denoted by circled dot (outward, for the edge atoms on the left) and circled cross (inward, for the edge atoms on the right), respectively. (b) The semi-infinite crack model. Atoms at the outer layer (in grey) are held fixed, while the remainder of the atoms is free.

II. MODELS AND METHODOLOGIES

A. The models

Monolayer graphene containing either a finite-sized edge crack (notch) or a semi-infinite crack is adopted as our simulation model, as shown in Fig. 1. The finite-sized crack model consists of a $6\text{nm} \times 6\text{nm}$ square monolayer graphene with a pre-existing notch created by removing a row of atoms from one of the graphene edges, as shown in Fig. 1(a). The notch separates the original edge into two short ones. Fixing the atoms along the two short edges (grey atoms in Fig. 1 (a)) while incrementally separating them in the opposite, out-of-plane directions effectively tears the graphene. At each separation, the system is dynamically relaxed to its minimal energy configuration. The Nose-Hoover's algorithm is employed to thermostat the system at 10K. We impose a fairly low separation speed ($0.0625\text{\AA}/\text{ps}$), which, along with the low temperature, mimics static free energy minimization. To simulate the invasion of external chemical additives, the edges of the notch and newly created fracture surfaces are terminated by oxygens or hydrogens prior to further crack extension, forming C-H single bonds and C/O bonds, respectively.

From the classical continuum fracture mechanics, there are three basic fracture modes: opening (Mode I), in-plane shear (Mode II), and out-of-plane shear (Mode III). Under a mixed mode loading (several modes coexist), the asymptotic stress at the crack tip can be generally written as:

$$\sigma_{ij}(r; \theta) = \sum_{M=I}^{III} \frac{K_M}{\sqrt{2\pi r}} \Lambda_{ij}^M(\theta) \quad (1)$$

where σ_{ij} is the stress tensor, i and j run over 1 to 2 representing the two coordinates (x, y) for the planar problem, r and θ are the two polar coordinates with the origin sitting at the crack tip; K is the stress intensity factor, M runs from I to III denoting the three fracture modes, respectively; Λ is the known angular dependent function for stress. Note that the stress presented in Eq. 1 is the leading term for very small r , i.e., the location at which the stress is evaluated is sufficiently close to the crack tip. The higher-order term is negligibly small compared to the leading term. The region within which the asymptotic stress is dominant is known as the K -dominant zone.

For bulk materials, tearing typically leads to pure Mode III fracture. However, when tearing a monolayer graphene, the tearing front is bent into the third dimension, same as tearing a thin film or a piece of paper. The bending mode arises for these thin-shell structures because of the large in-plane to out-of-plane stiffness ratio. As a result,

tearing of the graphene leads to a mixed mode at the crack tip. It has been well established that the crack-tip mode mixity greatly influences the fracture paths¹³. In order for studying the effects of load mixity on the fracture path in graphene, we introduce a size-reduced model that allows precise control of the load mixity, consisting of a small circular-shaped domain cut from the crack tip (Fig. 1(b)). The model simulates a semi-infinite crack that extends self-similarly. The domain size is chosen such that its outer boundary falls in the K -dominant zone. To impose an arbitrary mode mixity, we position all the atoms according to the crack-tip asymptotic displacement field:

$$u_i(r; \theta) = \sum_{M=I,III} \frac{2K_M}{\mu} \sqrt{\frac{r}{2\pi}} \Theta_i^M(\theta). \quad (2)$$

with specified K values, where μ is the shear modulus, Θ is the known angular dependent function for displacement. Then atoms about 3\AA from the outer boundary are held fixed, while the remaining atoms are dynamically relaxed at 10K. From continuum fracture mechanics, the imposed asymptotic displacement field results in the mixed mode stress field expressed in Eq. 1. It has also been previously shown that the atomic stress computed by the Virial formula agrees very well with the continuum asymptotic solution at the crack tip^{14,15}. Therefore, the semi-infinite model provides an effective scheme for the study of the effect of fracture mode mixity.

B. B. Interatomic potentials

In our MD simulations, the interatomic interactions are modeled by the reactive force field (ReaxFF)^{16,17}. The ReaxFF method combines a bond-distance/bond-order relationship with a geometry-dependent charge calculation, and provides a highly transferable method, applicable to covalent, metallic and ionic materials and their interfaces. The ReaxFF force field provides accurate account of bond breaking and bond formation in hydrocarbon-oxygen systems. Nonbonded interactions such as van der Waals and Coulomb interactions are calculated between each pair of atoms, irrespective of connectivity. However, close-range non-bonded interactions are excluded by using a shielding term. As tested on a number of hydrocarbon-oxygen systems, the ReaxFF has been adequately shown to give energies, reaction pathways, transition states, and reactivity trends that are in great agreement with quantum mechanical calculations and experiments^{18,19}, while capable of treating thousands of atoms. The ReaxFF force field has been widely used to study the graphene oxide²⁰, graphene peeling from a substrate²¹, and graphene ripping²².

III. III. RESULTS AND DISCUSSIONS

A. A. Direct MD observations of tearing paths

We first perform MD simulations of tearing the monolayer graphene using the finite-sized crack model. Our simulation results, as depicted in Fig. 2, clearly show the strong dependence of the fracture path on the chemical additives. In vacuum, the crack always extends along (if the original notch is of armchair edges) or kinks into (if the original notch is not of armchair edges) the armchair direction, independent of the initial notch orientation (Fig. 2(a)), consistent with previous tight-binding MD simulations²³. In the case of hydrogen invasion to the fractured surfaces, the fracture path remains the same as that in vacuum, and thus not shown here. In contrast, oxygenation of the fractured surfaces modifies the fracture path to the zigzag direction (Fig. 2(b)). Following these results, we simulated tearing of a GNR off a pristine graphene by creating two notches from one edge. As expected, a GNR with armchair edges is produced in vacuum (Fig. 2(c)) or in the presence of hydrogens (not shown), but with zigzag edges in the presence of oxygens (Fig. 2(d)), demonstrating the chemo-mechanical control of edge orientations in produced GNRs.

B. B. Tearing energetics and kinetics

We next examine the tearing energetics and kinetics in order to understand the modulating role of the chemo-mechanical conditions, focusing on the change in the fracture resistance in the presence of the chemical additives.

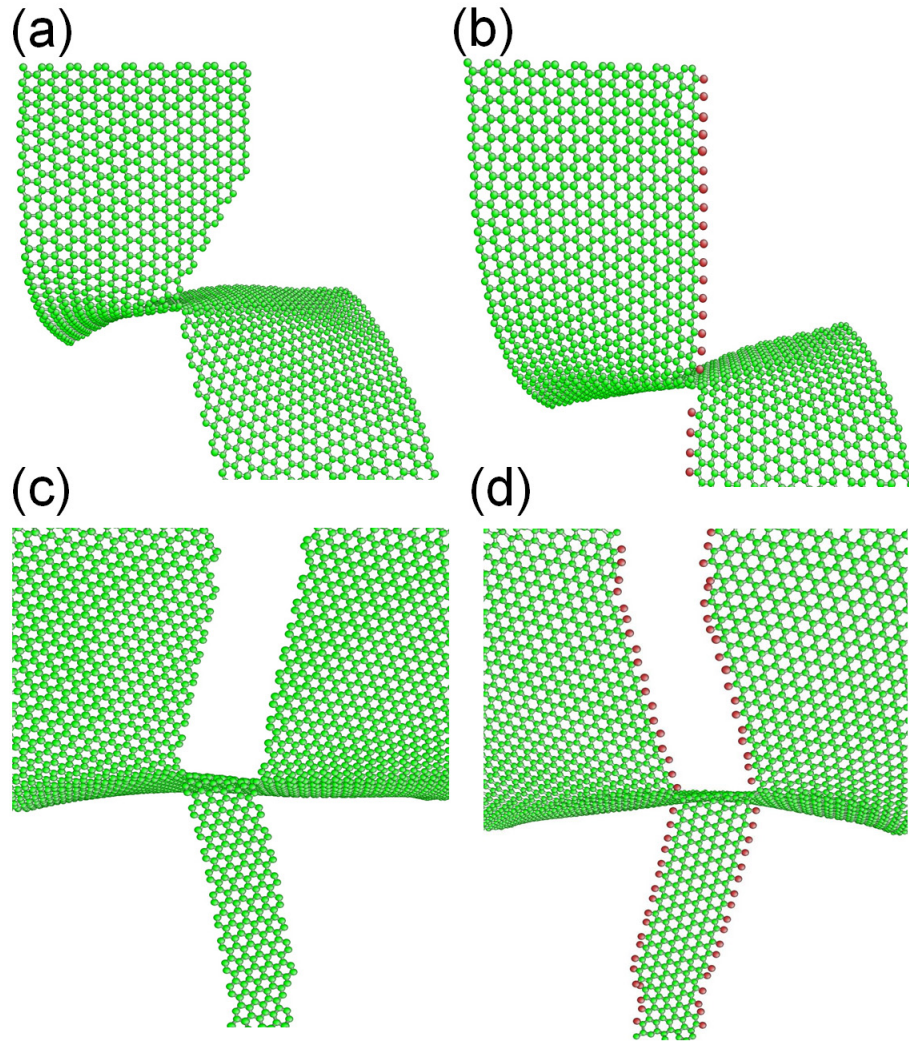


FIG. 2: Fracture paths in graphene determined by direct MD simulations, where red dots represent oxygens and green dots represent carbons. Tearing in vacuum or in the presence of hydrogens (not shown) causes notch extension along the armchair direction (a), but along the zigzag direction in the presence of oxygens (b). GNRs with edge orientations ((c) and (d)) corresponding to different chemical additives are produced by tearing off a graphene sheet with two initial notches.

Crack extension in crystals involves sequential bond breaking at the crack tip²⁴. From an energetics point of view, the unit process of bond breaking at the crack tip can be characterized by an energy landscape²⁵, as generically shown in Fig. 3(a). The energy landscape consists of two local energy minima that represent the two metastable states before and after bond breaking, separated by an energy barrier. The energy of a metastable state of an extending crack can be fully characterized by the crack length l and the applied load σ , i.e., $E(l; \sigma)$. The relative stability of the two metastable states with the same crack length depends on the applied load σ . At a relatively high (low) applied load the energy landscape tilts toward the bond-broken (bond-intact) state. The relative stability of the two metastable states indicates two critical loads for bond breaking. At the athermal load, the energy barrier against bond breaking vanishes, and the crack extends free of kinetic resistance. At the Griffith load²⁶, the two local energy minima are isoenergetic, and the crack extends free of thermodynamic resistance. Computationally, the athermal load, denoted by σ_A , can be determined by identifying the critical stress at which the bond-intact state is no longer numerically stable. Whereas the Griffith load, denoted by σ_G , can be determined by finding the critical stress at which the net change of the total energy of the system vanishes upon a unit crack extension by one lattice spacing:

$$\Delta E(\sigma_G) = E(l + a; \sigma_G) - E(l; \sigma_G) = 0 \quad (3)$$

where l is the crack length, and a is the lattice spacing along the crack extending direction. Due to the crystal anisotropy, both the Griffith and athermal loads may vary in different crystallographic directions. The energetically

(kinetically) preferred fracture path is then identified as the crystal direction with smaller Griffith (athermal) load.

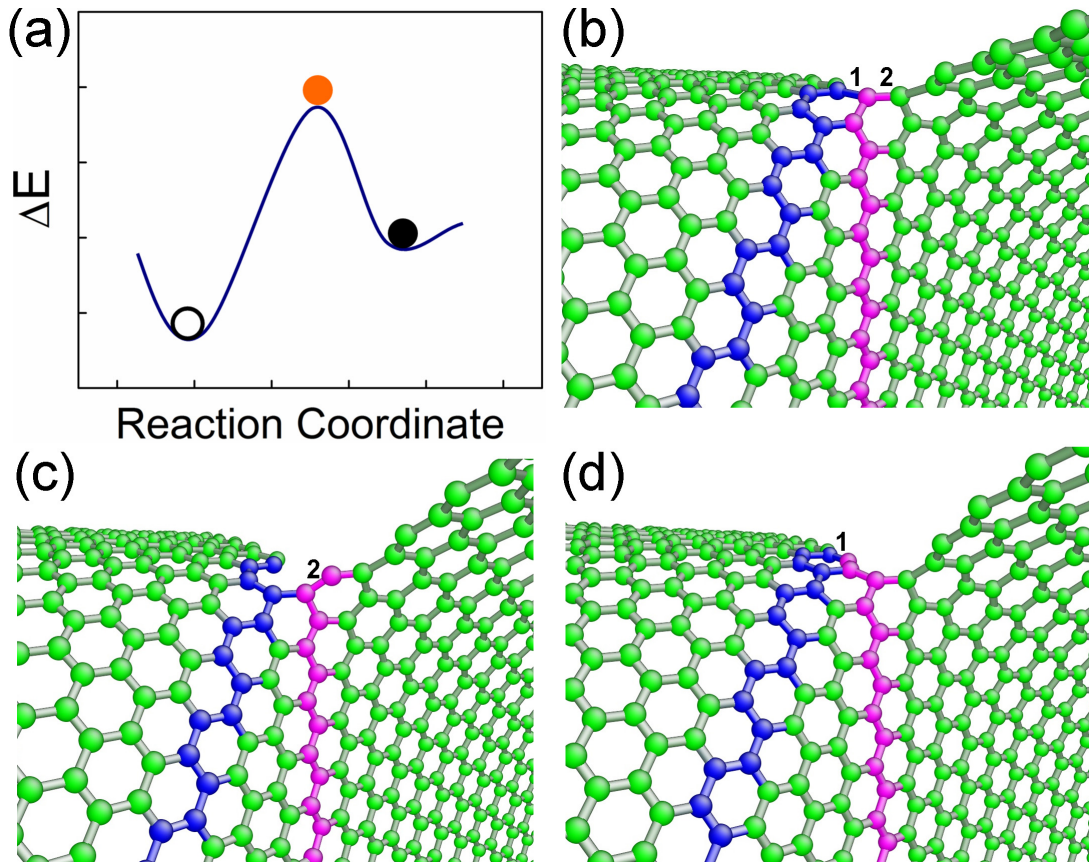


FIG. 3: Energetics and kinetics analyses of the unit bond breaking process illustrate crack kinking mechanisms in graphene. (a) A schematic description of the energy landscape for bond breaking at the crack tip. The energy difference between the filled black circle and the open circle gives rise to the thermodynamic driving force (ΔE) for bond breaking, while the energy difference between the filled yellow circle and the open circle to the kinetic barrier. (b) State A with two bonds (1 and 2) highlighted at crack tip, showing two possible crack extending directions (blue: armchair direction; pink: zigzag direction) by breaking each of the bonds; (c)-(d) State B (or C) is a replica of state A, but with bond 1 (or 2) broken. $A \rightarrow B$ (or $A \rightarrow C$) thus forms a unit bond-breaking process.

In order for determining and comparing the Griffith loads in two characteristic crystal directions (armchair and zigzag), we identify three metastable states along the two competing directions at the same applied load: a reference state $E_A(l; \sigma)$ (state A, Fig. 3(b)) with given crack surface orientation, the states with crack-tip bond broken along the armchair $E_B(l + a_{ac}; \sigma)$ (state B, Fig. 3(c)) and zigzag $E_C(l + a_{zz}; \sigma)$ (state C, Fig. 3(d)) directions, where a_{ac} and a_{zz} are respectively the lattice spacings along armchair and zigzag directions. The relative energetics of the three states defines the preferred fracture path: along armchair ($A \rightarrow B$) or zigzag ($A \rightarrow C$) directions.

We systematically computed the energies of these three metastable states via dynamic relaxation as a function of the applied load for both an initial armchair and zigzag notches, where the initial notch length is taken to be 15 \AA . We obtained the energy differences $\Delta E_1 = E_B - E_A$ and $\Delta E_2 = E_C - E_A$ along the armchair and zigzag directions as a function of the applied tearing displacement Δd , as plotted by the black and red curves in Fig. 4, respectively. The intersection between each curve and the dashed horizontal line ($\Delta E = 0$) indicates the Griffith displacement. The corresponding reaction force, i.e., the Griffith load, is listed in Table I. The subfigures in the first row are for an initial armchair notch, while those in the second row for an initial zigzag notch. In each row, the subfigures from left to right plot the energy differences in vacuum, in the presence of hydrogens, and in the presence of oxygens on the fracture surfaces, respectively.

If continuing increasing the applied load, one finds that at a critical load state A would no longer be numerically stable and automatically evolves to B or C. The corresponding applied load represents the athermal load along the direction to which state A evolves, and the athermal load in this direction is lower than that along the other direction.

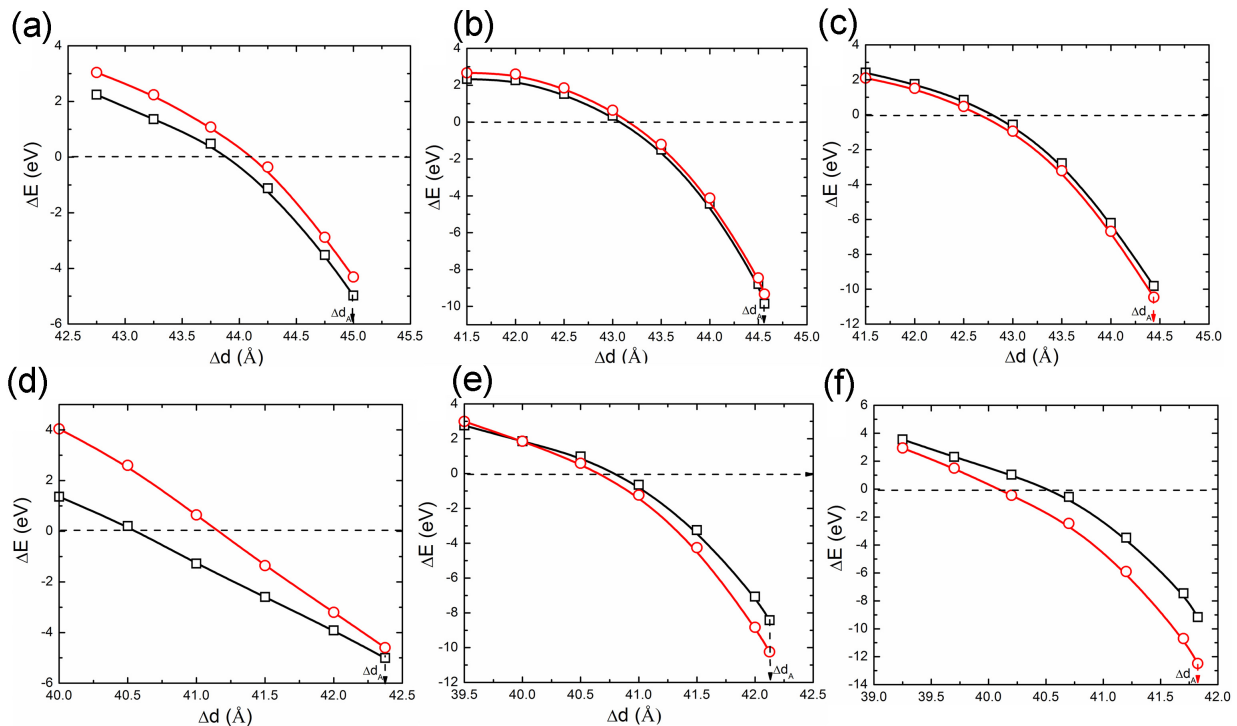


FIG. 4: Numerical determination of the Griffith load along different crystallographic directions. Figures (a) to (c) plot the energy differences in vacuum, in the presence of hydrogens, and in the presence of oxygens on the fracture surfaces respectively for an initial armchair notch. Figures (d) to (f) plot the energy differences in vacuum, in the presence of hydrogens, and in the presence of oxygens on the fracture surfaces respectively for an initial zigzag notch. Black curves: ΔE_1 ; Red curves: ΔE_2 .

In Fig. 4, the direction along which the lower athermal load is reached is indicated by an arrow. For instance, in Fig. 4 (a), the black arrow indicates the athermal load is reached first along the armchair direction for an initial armchair notch. The lower athermal loads in the three different chemical conditions are listed in Table I. Here only the lower athermal load is computed, since it suffices to identify the kinetically preferred fracture path. Direct determination of the higher athermal load along the other direction is not possible. However, it could be determined by first calculating the load-dependent energy barriers, followed by an extrapolation of the load-barrier curve to identify the maximum load at which the energy barrier vanishes, which by definition is the athermal load¹⁴

TABLE I: Fracture resistance against crack extension in graphene along different paths (unit: eV/nm^2). The higher athermal load is not computed, and marked by “-”s.

Fracture paths (Initial→ kinked)	In vacuum (σ_G/σ_A)	Oxygentated (σ_G/σ_A)	Hydrogentated (σ_G/σ_A)
AM→ AM	8.55/18.60	3.06/-	4.74/17.85
AM→ ZZ	9.30/-	2.31/17.48	5.74/-
ZZ→ AM	1.02/19.04	5.12/-	8.93/17.73
ZZ→ ZZ	1.59/-	3.18/16.85	7.12/-

Table I lists the Griffith load and athermal load at different chemical conditions along different fracture paths. Each path is constituted of an initial and a final direction, where “AM” denotes armchair direction, while “ZZ” denotes zigzag direction. Our simulation results show that in vacuum both the Griffith and athermal loads along the armchair direction is consistently lower than those along the zigzag direction, independent of the initial notch orientation, clearly demonstrating that the armchair fracture path is energetically favorable. In the presence of oxygens to the fracture surfaces, the preferred fracture path changes to the zigzag direction, also independent of the initial crack orientation. In contrast, in the presence of hydrogens, the athermal load is always lower in the armchair direction, same as that in vacuum. Interestingly, the lower Griffith load always occurs along the initial notch direction, showing

the dependence of the energetically favorable fracture paths on the initial crack orientation.

C. C. Effects of load mixity

The Griffith and athermal loads represent the intrinsic fracture resistances along specified fracture paths. We next discuss the effects of loading conditions on the fracture paths. As mentioned earlier, tearing a bulk material results in pure Mode III stress at the crack tip, as shown in Fig. 5(a). In contrast, tearing a monolayer graphene results in bending at the crack tip due to the large in-plane to out-of-plane stiffness ratio. Thus, the fracture mode expressed at the crack tip may deviate from the pure Mode III, introducing crack-tip mode mixity¹³. To determine the crack-tip fracture modes, we computed the Virial stress at each atomic position and interpolated the stress over the entire simulation domain, as shown in Fig. 5(b). At low temperatures, the kinetic component of the Virial stress is negligibly small, and the Virial stress tensor σ can be expressed as:

$$\sigma = \frac{1}{2\Omega} \sum_{j \neq i} \mathbf{r}_{ij} \otimes \mathbf{f}_{ij}, \quad (4)$$

where i and j are the indices of interacting atom neighbors, and Ω is taken to be the area occupied by an atom in the initial, undeformed state; $\mathbf{r}_{ij} = \mathbf{r}_j - \mathbf{r}_i$ is the distance vector between atoms i and j . The interatomic force \mathbf{f}_{ij} can be written as

$$\mathbf{f}_{ij} = \frac{\partial \Phi}{\partial r_{ij}} \frac{\mathbf{r}_{ij}}{r_{ij}}. \quad (5)$$

where Φ is the interaction potential. The calculated Virial stress at each atomic site is then interpolated over the entire simulation domain. Figure 5(b) plots the interpolated stress component σ_{13} . By comparison, we find the Virial stress component significantly deviates from the corresponding asymptotic stress of pure Mode III, indicating a mixed mode at the crack tip. We then computed other stress components in addition to those in pure mode III (σ_{13} and σ_{23}). Regression analysis of the Virial stress components based on the asymptotic crack tip stress distribution function (Eq. 1) gives rise to the K values of the three modes. Our calculation shows that $K_I/K_{III} = 2.71$ and $K_{II}/K_{III} = 0.04$ in the tearing specimen, manifesting mode I, rather than mode III, is the dominant fracture mode at the crack tip.

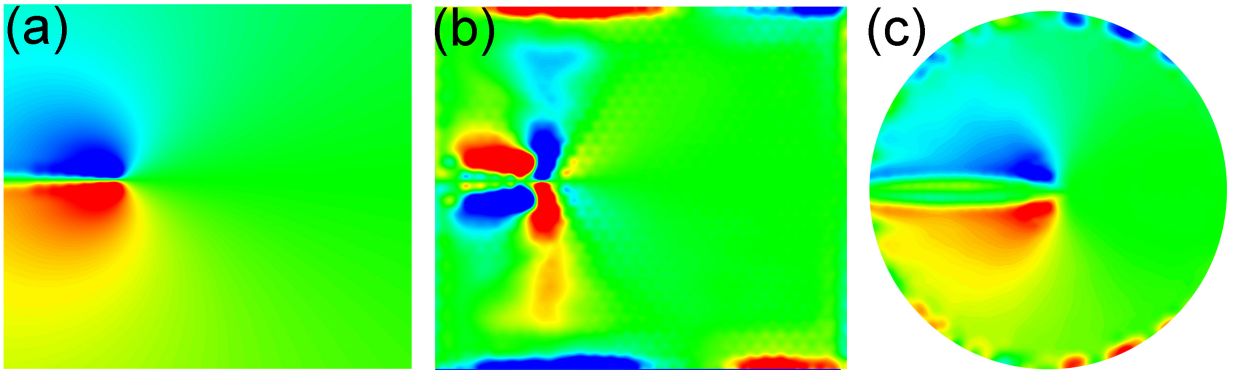


FIG. 5: Crack-tip stress (σ_{13}) distribution suggests mode mixity. Red (blue) color represents positive (negative) stresses. (a) Continuum asymptotic solution of pure mode III; (b) the finite-size tearing model; (c) the size-reduced model with pure mode III loading.

we next utilize the semi-infinite crack model (Fig. 1(b)) to identify the role of the load mixity in the fracture path. This model enables continuous variation of the mode mixity over the entire spectrum. At specified K_M ($M = I, II, III$), the atoms in the model are displaced according to the asymptotic displacement field in Eq. (2). The Virial stress at each atomic site is then calculated upon the system is dynamically relaxed at 10K. For consistency, here Mode II is not included ($K_{II} = 0$) since Mode II is negligibly small as compared to other modes in the finite-sized crack model. The mode mixity ϕ is defined by $K_I + K_{III}i = Ke^{i\phi}$, ranging from 0 (pure mode III) to $\pi/2$ (pure mode I). Figure

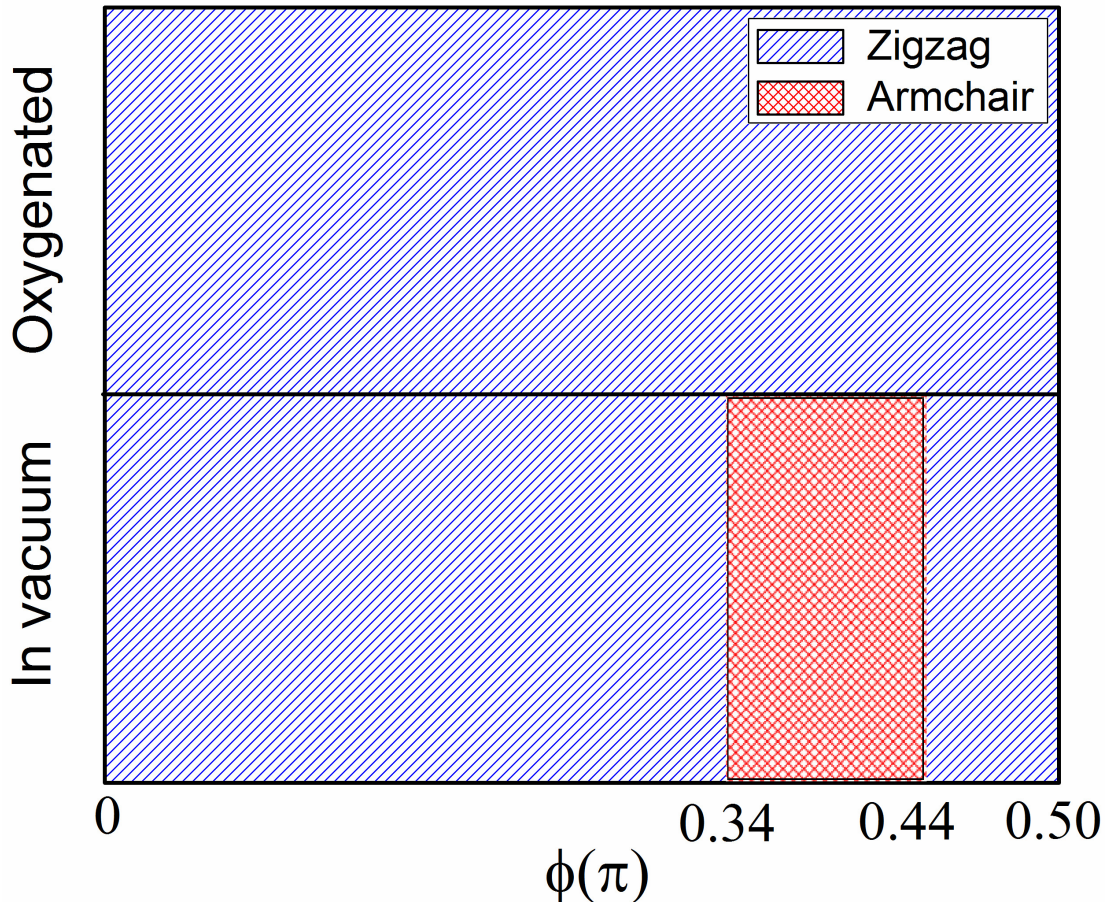


FIG. 6: A map of the preferred fracture paths in the plane of chemical condition and crack-tip mode mixity ϕ . The preferred fracture paths are shaded differently (slashed for zigzag direction, and cross-hatched for armchair).

5(c) plots the Virial stress σ_{13} for $\phi = 0$. Its close agreement to the asymptotic stress (Eq. (1), Fig. 5(a)) validates the size-reduced model.

We determine the kinetically preferred fracture path at different mode mixities by direct MD simulations, i.e., the path with a lower athermal load. Our simulations showed that in the case of in vacuum or in the presence of oxygens, the determined path is also thermodynamically preferred, i.e., with a lower Griffith load. A map of preferred fracture paths (either zigzag or armchair, denoted by differently shaped regions) is depicted in Fig. 6, where the horizontal axis denotes the mode mixity and the vertical axis the chemical conditions. In vacuum, zigzag direction is the preferred fracture path when ϕ falls in the range of $[0, \sim 0.34\pi)$ or $(\sim 0.44\pi, \pi/2]$. For other ϕ values, fracture along armchair direction becomes favored. In contrast, in the presence of oxygens, armchair direction is always the preferred fracture path regardless of the imposed mode mixity, showing the dominant role of the oxygenation induced fracture resistance.

We would like to point out that invasion kinetics of chemical additives falls beyond the scope of the present study. Instead, in our simulations the chemical additives are continuously supplied to the crack tip to terminate the dangling bonds, whenever new fracture surfaces are produced. The underlying assumption is that the crack extending speed is sufficiently slow as compared to the invasion rate of the chemical additives. The invasion rate of the external molecules to the crack tip depends on the association barriers and the applied pressure, while the crack propagation speed depends on the kinetic barrier of bond breaking at the crack tip and thus the applied load¹⁴; both are tunable experimental conditions. Therefore, in theory our assumption of continuous termination of dangling bonds by invading chemical additives can be satisfied by manipulating the relevant experimental conditions.

IV. IV. CONCLUSIONS

In summary, our MD simulations showed the regulatory role of chemo-mechanical conditions on the fracture path when tearing a monolayer graphene. On the one hand, the presence of chemical additives modifies the fracture resistance to an extent depending on the crystal directions. On the other, due to the extremely large ratio of the out-of-plane bending modulus to the in-plane stretching modulus, tearing graphene results in mode mixity local to the crack tip, which also affects the fracture path. Nevertheless, our systematic studies evidenced that the fracture paths can be effectively regulated by chemo-mechanical conditions, thereby offering a new pathway for atomic engineering of GNRs with controlled edge orientations. The chemo-mechanics origins of GNR edge structures produced by tearing monolayer graphene thus shed light on the design of graphene-based next-generation electronic devices.

We thank J. Buehler at MIT for helpful discussions. X.H. and S.Z. acknowledge the support by the National Science Foundation.

* Electronic address: suz10@psu.edu

- ¹ K. S. Novoselov, E. McCann, S. V. Morozov, V. I. Fal'ko, M. I. Katsnelson, U. Zeitler, D. Jiang, F. Schedin, and A. K. Geim, *Nat. Phys.* **2**, 177–180 (2006).
- ² Y. B. Zhang, Y. W. Tan, H. L. Stormer, and P. Kim, *Nature* **438**, 201–204 (2005).
- ³ K. S. Novoselov, Z. Jiang, Y. Zhang, S. V. Morozov, H. L. Stormer, U. Zeitler, J. C. Maan, G. S. Boebinger, P. Kim, and A. K. Geim, *Science* **315**, 1379–1379 (2007).
- ⁴ X. Li, X. Wang, L. Zhang, S. Lee, and H. Dai, *Science* **319**, 1229–1232 (2008).
- ⁵ V. B. Shenoy, C. D. Reddy, A. Ramasubramaniam, and Y. W. Zhang, *Phys. Rev. Lett.* **101**, 245501 (2008).
- ⁶ L. Ci, Z. P. Xu, L. L. Wang, W. Gao, F. Ding, K. F. Kelly, B. I. Yakobson, and P. M. Ajayan, *Nano Res.* **1**, 116–122 (2008).
- ⁷ J. Y. Huang, F. Ding, B. I. Yakobson, P. Lu, L. Qi, and J. Li, *Proc. Natl. Acad. Sci. USA* **106**, 10103–10108 (2009).
- ⁸ M. Y. Han, B. Ozyilmaz, Y. B. Zhang, and P. Kim, *Phys. Rev. Lett.* **98**, 206805 (2007).
- ⁹ S. Stankovich, R. D. Piner, S. T. Nguyen, and R. S. Ruoff, *Carbon* **44**, 3342–3347 (2006).
- ¹⁰ A. P. Yu, P. Ramesh, M. E. Itkis, E. Bekyarova, and R. C. Haddon, *J. Phys. Chem. C* **111**, 7565–7569 (2007).
- ¹¹ A. Dimiev, D. V. Kosynkin, A. Sinitskii, A. Slesarev, Z. Sun, and J. M. Tour, *Science* **331**, 1168–1172 (2011).
- ¹² C. Lee, X. D. Wei, J. W. Kysar, and J. Hone, *Science* **321**, 385–388 (2008).
- ¹³ A. G. Varias, Z. Suo, and C. F. Shih, *J. Mech. Phys. Solids* **40**, 485–509 (1992).
- ¹⁴ S. Zhang, T. Zhu, and T. Belytschko, *Phys. Rev. B* **76**, 094114 (2007).
- ¹⁵ T. Zhu, J. Li, and S. Yip *Phys. Rev. Lett.* **93**, 025503 (2004).
- ¹⁶ A. C. T. van Duin, S. Dasgupta, F. Lorant, and W. A. Goddard III, *J. Phys. Chem. A* **105**, 9396–9409 (2001).
- ¹⁷ K. Chenoweth, S. Cheung, A. C. T. van Duin, W. A. Goddard III, and E. M. Kober, *J. Am. Chem. Soc.* **127**, 7192–7202 (2005).
- ¹⁸ A. Strachan, E. M. Kober, A. C. T. van Duin, J. Oxgaard, and W. A. Goddard III, *J. Chem. Phys.* **122**, 054502 (2005).
- ¹⁹ K. Chenoweth, A. C. T. van Duin, W. A. Goddard III, *J. Phys. Chem. A* **112**, 1040–1053 (2008).
- ²⁰ A. Bagri, C. Mattevi, M. Acik, Y. J. Chabal, M. Chhowalla, and V. B. Shenoy, *Nat. Chem.* **2**, 581–587 (2010).
- ²¹ D. Sen, K. S. Novoselov, P. M. Reis, and M. J. Buehler, *Small* **6**, 1108–1116 (2010).
- ²² K. Kim, V. I. Artyukhov, W. Regan, Y. Liu, M. F. Crommie, B. I. Yakobson, and A. Zettl, *Nano Lett.* **12**, 293–297 (2012).
- ²³ T. Kawai, S. Okada, Y. Miyamoto, and H. Hiura, *Phys. Rev. B* **80**, 033401 (2009).
- ²⁴ R. Thomson and C. Hesieh, and V. Rana, *J. Appl. Phys.* **42**, 3154–3160 (1971).
- ²⁵ W. A. Curtin, *J. Mater. Res.* **5**, 1549–1560 (1990).
- ²⁶ A. A. Griffith, *Philos. Trans. R. Soc. London, A* **221**, 163 (1920).